Int J Adv Manuf Technol (2016) 84:2449–2460
DOI 10.1007/s00170-015-7888-2

ORIGINAL ARTICLE

An analytical force model for ball-end milling based on a predictive machining theory considering cutter runout

Zhongtao Fu[1] · **Wenyu Yang**[1] · **Xuelin Wang**[1] · **Jürgen Leopold**[1,2]

Received: 13 July 2015 / Accepted: 21 September 2015 / Published online: 3 October 2015

Abstract The work is motivated by the fact that cutting forces are commonly calculated by the mechanistic or numerical models which are considered time-consuming and impractical for various cutting conditions and workpiece-tool pair, and the irregular distribution of cutting forces is generated due to the uneven redistribution of the instantaneous uncut chip thickness (IUCT) caused by the cutter runout in ball-end milling process. Therefore, this paper presents an analytical force model considering the cutter runout for ball-end milling based on a predictive machining theory, which regards the workpiece material properties, tool geometry, cutting conditions, and types of milling as the input data. In this model, the shear flow stress is estimated by introducing a modified Johnson-Cook constitutive law which considers the phenomenon of the work hardening, temperature softening, and material size-effect. Each cutting edge of the ball-end cutter is discretized into a series of infinitesimal elements along the cutter axis and the cutting action of which is equivalent to the classical oblique cutting process. Thus, the cutting force components applied on each element can be calculated using a predictive oblique cutting model and the total instantaneous cutting forces are obtained by summing up the forces contributed by all cutting edges. What is more, this model takes into account the effect of the edge radius, varying sliding friction coefficient and cutter runout on the cutting forces. Finally, the proposed analytical model of cutting forces is verified by the published results and experimental data. Good agreement shows the effectiveness of the proposed analytical model and highlights the importance of the cutter runout on the forces.

Keywords Analytical force model · Ball-end milling · Predictive machining theory · Cutter runout

1 Introduction

Ball-end milling is extensively used in the manufacturing of sculptured free-form surfaces, such as propellers, turbines, and dies/molds. Modeling of cutting forces is the basis for the prediction of tool wear and breakage, machine-tool vibration, cutting parameters optimization, and surface quality [1, 2]. It is also well known that the amplitude and distribution of cutting forces are greatly influenced by cutter runout which is a common phenomenon in multi-fluted milling process [3]. Therefore, establishing a reliable force model is an important research topic to ensure the prediction accuracy of cutting forces.

Literature review shows that there have been many force models developed to predict the cutting forces in milling processes. The mechanistic models are commonly available to predict cutting forces, in which the cutting coefficients are calibrated using the empirical curve fit from a set of milling experiments [4–8] or orthogonal/oblique cutting data [9–12] for a given tool-workpiece pair. Despite the increased sophistication and usefulness of the developed mechanistic models for studying the cutter deflection and runout, surface errors, chatter vibrations, and federate optimization [13–16], the

✉ Wenyu Yang
mewyang@hust.edu.cn

[1] State Key Laboratory of Digital Manufacturing Equipment and Technology, School of Mechanical Science and Engineering, Huazhong University of Science and Technology, Wuhan 430074, China

[2] TBZ-PARIV GmbH, Chemitz 09661, Germany

models are only valid for a certain workpiece-tool material pair and the cutting coefficients calibration done by numerous experiments is fastidious due to high cost and hardware setup complexity. To avoid such limitations, extensive research effort has been sacrificed to develop the analytical models for the prediction of cutting forces.

Merchant et al. [17] and Armarego et al. [18] are the initial contributors to the analytical models for predicting cutting forces by the orthogonal and oblique cutting mechanics, which was independent of the experimental calibration and can be applied to the complex milling process. Based on the slip-line field analysis, Oxley [19] developed a predictive machining theory that considers the work hardening and thermal softening of workpiece material and the cutting forces can be determined by the flow stress of the workpiece material. Application of the Oxley's theory and its extended form [20] has achieved success to the simulation of end milling and face milling in the work of Young et al. [21], Li et al. [22, 23], Zheng et al. [24], and Pang [25]. Furthermore, through introducing the thermo-mechanical behavior of the workpiece material and the tool-chip interface friction characteristics, Moufki et al. [26], Li et al. [27], and Fu et al. [28] also presented a predictive force model for helical end milling process using the oblique cutting approach. These analytical models provide a simple and efficient approach to predict the cutting forces based on the predictive machining theory, which are also valid for various cutting conditions and workpiece-tool pair with avoidance of laborious experimental works.

As mentioned above, compared to other force models, the analytical force models present major advantages and may be dominated in future advances of metal cutting modeling reviewed by Arrazola et al. [29]. In a recent work by the authors' group [28], an analytical force model for predicting cutting forces in helical end milling was proposed. However, this model used the simplified Johnson-Cook constitutive law and expression of shear angle and did not consider the effect of cutter runout, which could affect the prediction accuracy of the cutting forces. What is more, the chip geometry, through the ball-end milling process, is not constant due to the continually changing and highly complicated cutter geometry of ball-end milling compared with helical end milling, which thereby making the force analysis much more complex. Therefore, the purpose of this paper is to develop an analytical force model with cutter runout for ball-end milling using the classic oblique cutting approach based on the non-equidistant shear zone mode proposed by Li et al. [30]. In this model, the shear flow stress is estimated by introducing a modified Johnson-Cook constitutive law which considers the phenomenon of the work hardening, temperature softening, and material strengthening. Furthermore, a generalized algorithm is presented to calculate instantaneous uncut chip thickness (IUCT) with cutter runout. The cutting edge of ball-end milling is discretized into a series of infinitesimal elements, and the corresponding differential forces applied on each infinitesimal element are predicted analytically using the oblique cutting approach. Besides, the investigation of the material strengthening and varying sliding friction coefficient on cutting forces is also carried out to provide better understanding for ball-end milling.

The organization of this paper is as follows: After introducing the geometry of the cutter and the expression of the related parameters in ball-end milling process in Section 2, an analytical force model for ball-end milling is proposed by regarding the cutting action of each slice on the cutting edge as the classical oblique cutting process in which the force components can be calculated based on the predictive machining theory. Moreover, the cutter runout is also investigated in Section 3. The model validation is implemented and discussed in Section 4 by the published results available in the literature and the experimental data. Finally, conclusions of this study are drawn in Section 5.

2 Geometry of ball-end milling

The global geometry of the ball-end mill is derived from the generalized mill model by assigning special values to seven parameters, D, R, R_r, R_z, α, β, and H, defined in a generalized cutter [6], which is shown in Fig. 1a. The related parameters are defined in TCS (tool coordinate system) $\{O-XYZ\}$ linked to the cutter tip. The helical cutting edges are wrapped around the cutter envelope surface which consists of two separated zones: the spherical surface OS with variable helix angle and cylindrical surface SN with constant lead and radius R_0.

In Fig. 1a, the point P on the j-th cutting edge with elevation z is located by the periphery radius $R(z)$, the radial immersion angle $\varphi_j(z)$, and the axial immersion angle $\kappa(z)$. And these three parameters are evaluated as follows:

The periphery radius $R(z)$ is obtained by:

$$R(z)=\begin{cases}\sqrt{{R_0}^2-(R_0-z)^2} & 0\le z<R_0\\ R_0 & z\ge R_0\end{cases} \tag{1}$$

The radial immersion angle $\varphi_j(z)$ is measured clockwise from the positive Y-axis to a reference cutting edge $j=1$ and defined by:

$$\varphi_j(z)=\varphi+(j-1)\frac{2\pi}{N_t}-\psi(z) \tag{2}$$

where N_t is the number of cutting edges, φ is the tool rotation angle, and $\psi(z)$ is the radial lag angle and expressed as:

$$\psi(z)=\begin{cases}\frac{z}{R(z)}\tan i(z) & 0\le z<R_0\\ \frac{z}{R_0}\tan i_0 & z\ge R_0\end{cases} \tag{3}$$

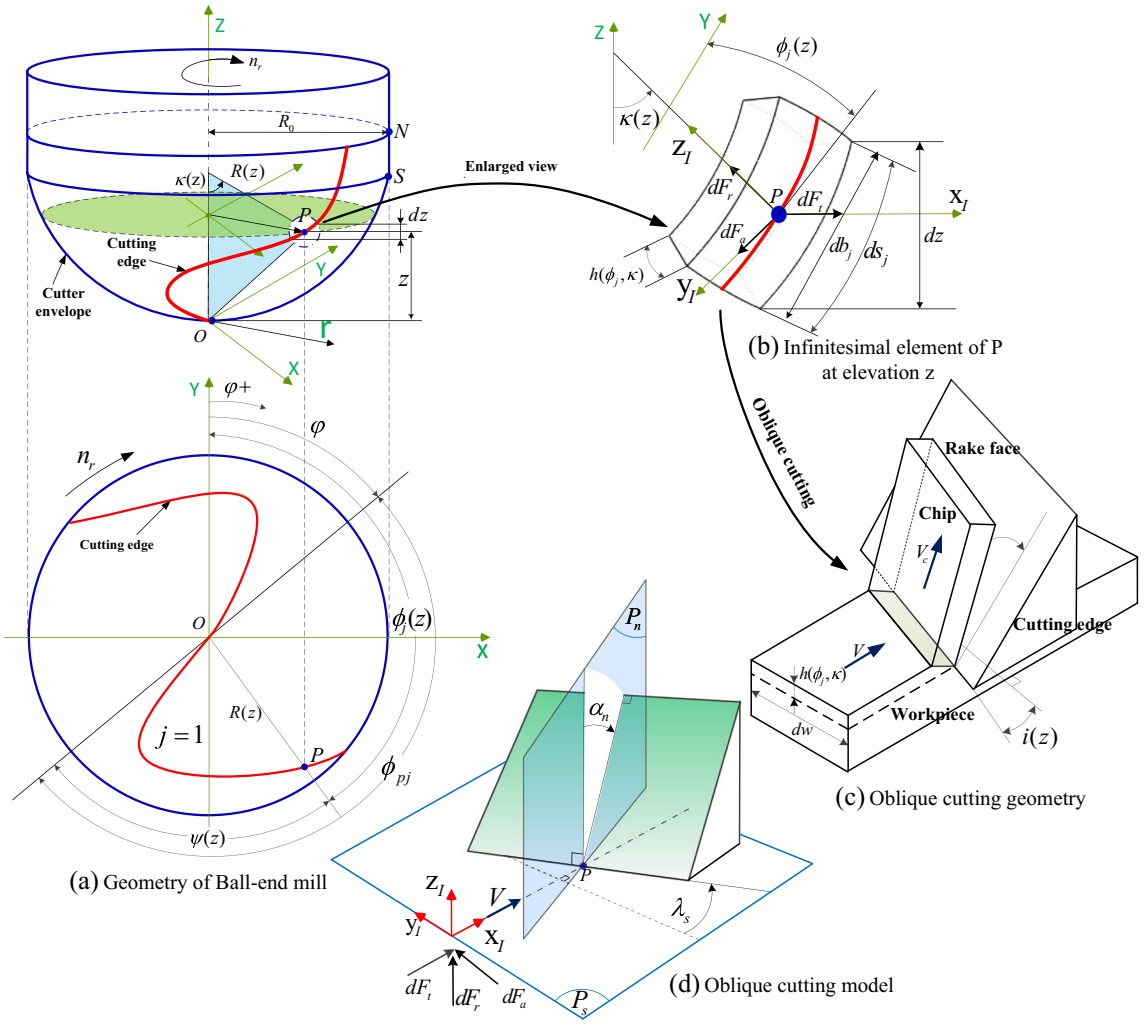

Fig. 1 Geometry of the ball-end mill and oblique cutting model of the infinitesimal element

The axial immersion angle $\kappa(z)$ is defined as the angle between the cutter axis and normal of cutting edge at point P and can be written as:

$$\kappa(z) = \begin{cases} cos^{-1}\left(\frac{R_0 - z}{R_0}\right) & 0 \le z < R_0 \\ \pi/2 & z \ge R_0 \end{cases} \tag{4}$$

For the helix angle $i(z)$, it varies along the cutting edge due to the change of periphery radius and is defined by:

$$i(z) = \boldsymbol{tan^{-1}}\left(\frac{R(z)}{R_0}\tan i_0\right) \tag{5}$$

where i_0 is the constant helix angle on the cylindrical part of the ball-end mill.

From the previous works [1], the cutting edges of ball-end cutter can be decomposed into a series of infinitesimal oblique cutting elements corresponding to the axial increment dz, and the calculation of cutting forces acting on each cutting edge requires the identification of cutting velocity, infinitesimal cutting edge geometry, chip load, and IUCT. For the infinitesimal element of point P on the j-th cutting edge with elevation z shown in Fig. 1b, the IUCT $h(\varphi_j,\kappa)$ changes with both radial φ_j and axial immersion κ and is given by:

$$h(\varphi_j, \kappa) = f_{t,j}\sin\varphi_j \sin\kappa \tag{6}$$

where $f_{t,j}$ is the feed per tooth.

The width of cut db_j is the projected length of the infinitesimal element along the direction of cutting velocity V and expressed as:

$$db_j = dz/\sin(\kappa) \tag{7}$$

The infinitesimal arc length ds_j is given as [6]:

$$ds_j = dz\sqrt{\left(R(z)\psi'(z)\right)^2 + \left(R'(z)\right)^2 + 1} \tag{8}$$

where ' denotes the derivation with respect to z.

As shown in Fig. 1c, the three cutting forces (dF_t, dF_r, dF_a) of the infinitesimal element at point P can be derived from the

oblique cutting model. In this model, the related parameters and planes are defined in LCS (local coordinate system) $\{P, x_l, y_l, z_l\}$. P_s is the cutting plane, P_n is the normal plane, and α_n is the normal rake angle measured in P_n and defined as [10]:

$$\alpha_n = \tan^{-1}(\tan\alpha_r \cos i) \tag{9}$$

where α_r is the radial rake angle.

The inclination angle λ_s is measured between the cutting edge and the normal direction to the cutting velocity in P_s and defined as:

$$\lambda_s = \tan^{-1}(\tan i \sin\kappa) \tag{10}$$

In addition, the local cutting velocity $V = 2\pi n_r \cdot R(z)$, where n_r is the spindle speed.

3 Modeling of milling forces

3.1 Oblique cutting model

For application to cutting forces modeling of ball-end milling, the cutting action of each infinitesimal element can be represented as the oblique cutting process. And the relevant equations derived from the oblique cutting model [27] (Fig. 2) are established and summarized.

To study this process, an equivalent plane P_e, which is determined by the cutting velocity V and chip velocity V_c, is introduced in this model so that the mechanism of oblique cutting is regarded as a two dimensional cutting process (plane plastic flow state) [19]. According to the coordinate transform and oblique geometric relation in Fig. 2a, three essential parameters are summarized as follows:

The equivalent plane angle η_e, which determines the equivalent plane P_e, is [27]:

$$\eta_e = \tan^{-1}\left(\frac{\tan\eta_c \cos\eta_{sh} + \sin(\varphi_n - \alpha_n)\sin\eta_{sh}}{\cos(\varphi_n - \alpha_n)}\right) \tag{11}$$

The shear flow angle η_{sh} which characterizes the shear direction in primary shear zone are given by [26, 28]:

$$\eta_{sh} = \tan^{-1}\left(\frac{\tan\lambda_s \cos(\varphi_n - \alpha_n) - \tan\eta_c \sin\varphi_n}{\cos\alpha_n}\right) \tag{12}$$

The chip flow angle η_c on the rake face A_γ, assuming that the chip velocity and the friction are collinear, is calculated from the following implicit equation [26]:

$$\begin{aligned}&\tan\lambda_s \tan\beta_n \cos(\varphi_n - \alpha_n)\sin(\varphi_n - \alpha_n)\cos^2\eta_c - \tan\lambda_s \cos^2(\varphi_n - \alpha_n)\\ &+\tan\eta_c \sin\varphi_n \cos(\varphi_n - \alpha_n) + (\cos\alpha_n - \sin\varphi_n \sin(\varphi_n - \alpha_n))\sin\eta_c \tan\beta_n = 0\end{aligned} \tag{13}$$

In Fig. 2b, the primary shear zone is modeled as a parallel and non-equidistant shear band of thickness $\hbar$ which consists of two non-equidistant thickness $(1-\chi)\hbar$ and $\chi\hbar$, characterized by the portion $\in[0, 1]$ The governing equations for the shear strain rate $\dot{\gamma}$, the shear strain γ, the temperature T, and the maximum shear strain rate $\dot{\gamma}_m$ in the primary shear zone are detailed in [28] and are given as:

$$\dot{\gamma} = \begin{cases} \dfrac{\dot{\gamma}_m}{[(1-\chi)\hbar]^q}[z_e + (1-\chi)\hbar]^q & z_e \in [-(1-\chi)\hbar, 0] \\ \dfrac{\dot{\gamma}_m}{(\hbar)^q}(\chi\hbar - z_e)^q & z_e \in [0, \chi\hbar] \end{cases} \tag{14}$$

$$\gamma = \begin{cases} \dfrac{\cos\eta_e \dot{\gamma}_m}{V\cos\lambda_s \sin\varphi_n (q+1)[(1-\chi)\hbar]^q}[z_e + (1-\chi)\hbar]^{q+1} & z_e \in [-(1-\chi)\hbar, 0] \\ -\dfrac{\cos\eta_e \dot{\gamma}_m (\chi\hbar - z_e)^{q+1}}{V\cos\lambda_s \sin\varphi_n (q+1)(\chi\hbar)^q} + \dfrac{\cos\eta_e \cos\alpha_n}{\sin\varphi_n \cos\eta_s \cos(\varphi_n - \alpha_n)} & z_e \in [0, \chi\hbar] \end{cases} \tag{15}$$

$$\frac{\partial T}{\partial z_e} = \frac{\cos\eta_e}{\rho_m C_p V \cos\lambda_s \sin\varphi_n} \chi\tau\ \dot{\gamma} \tag{16}$$

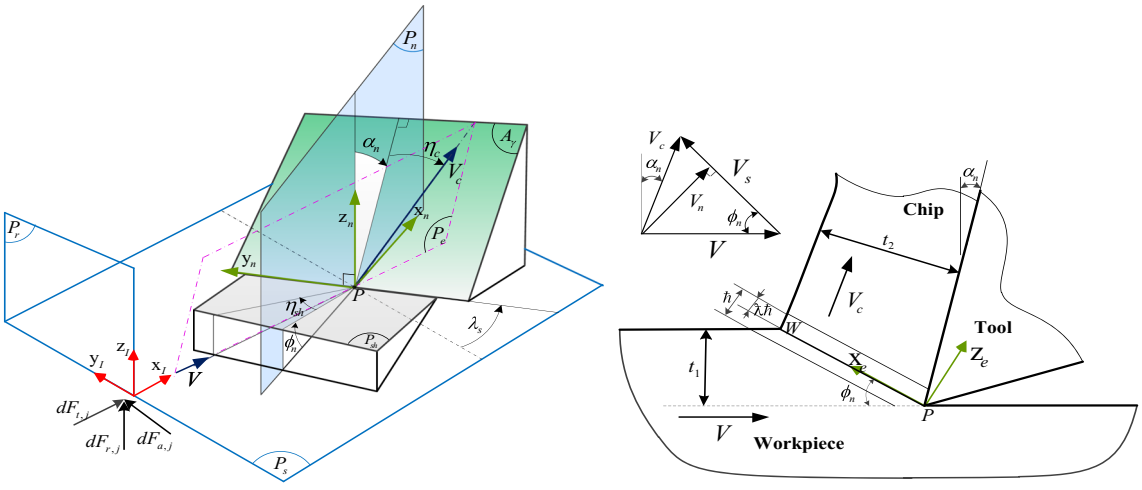

(a) Oblique cutting model and chip formation (b) Non-equidistant shear model

Fig. 2 Oblique cutting model and chip formation of infinitesimal cutting edge

$$\dot{\gamma}_m = \frac{(q+1)V\cos\lambda_s\cos\alpha_n}{\hbar\cos\eta_{sh}\cos(\varphi_n-\alpha_n)} = \frac{(q+1)V_s}{\hbar} \tag{17}$$

$$\chi = 1-\frac{\cos\eta_{sh}\cos(\varphi_n-\alpha_n)(cos\varphi_n\cos\eta_{sh}+\tan\lambda_s\sin\eta_{sh})}{\cos\alpha_n} \tag{18}$$

$$V_c = \frac{V\cos\lambda_s\sin\varphi_n}{\cos\eta_c\cos(\varphi_n-\alpha_n)}, \quad V_s = \frac{V\cos\lambda_s\cos\alpha_n}{\cos\eta_s\cos(\varphi_n-\alpha_n)} \tag{19}$$

where ρ_m is the material density, C_p is the heat capacity, and χ is the Taylor-Quinney coefficient.

The normal friction angle β_n was analyzed and extended to the oblique cutting by Budak et al. [31] who presented an analytical dual-zone model of the tool-chip interface. And the formula of β_n can be derived as follows:

$$\mu_f = \tan\beta_n = \frac{\tau_s}{P_0}\left(1+\xi\left(1-\left(\frac{\tau_s}{\mu_s P_0}\right)^{1/\xi}\right)\right) \tag{20}$$

where $P_0 = 4\frac{\xi+1}{\xi+2}\frac{\cos^2\beta_n\cos\eta_{sh}}{\sin[2(\varphi_n+\beta_n-\alpha_n)]}\tau_s$ is the normal pressure at tool tip; ξ is the exponent for pressure distribution taken as 3; μ_f and μ_s are the mean friction coefficient and the sliding friction coefficient, respectively, on the tool-chip interface. However, μ_s may be not constant due to the variation of the chip velocity in ball-end milling, and it decreased drastically as the chip velocity increased reported in [32].

Normal shear angle φ_n, as a key parameter to calculate the shear force, is determined by a modified Merchant equation [17]:

$$\varphi_n = C_1-C_2(\beta_n-\alpha_n) \tag{21}$$

where C_1 (in rad) and C_2 are constant depending on the workpiece-tool material. And the special values $C_1 = \pi/4, \quad C_2 = 0.5$ have been obtained based on the minimum energy principle for mild steel work and carbide tool.

The workpiece material is supposed to be isotropic and viscoplastic-rigid, and its shear flow stress τ_{JC} is described by the Johnson-Cook constitutive law as follows:

$$\tau_{JC} = \frac{1}{\sqrt{3}}\left(A+B\left(\frac{\gamma}{\sqrt{3}}\right)^n\right)\left(1+C\ln\left(\frac{\dot{\gamma}}{\dot{\gamma}_0}\right)\right)\left(1-\left(\frac{T-T_r}{T_m-T_r}\right)^m\right) \tag{22}$$

where $\dot{\gamma}_0, T_r, T_m$ represent reference shear strain rate, room temperature, and melting temperature, respectively. The characteristics of material behavior are strain hardening exponent n, strain rate sensitivity coefficient C, thermal softening coefficient m, yield strength A, and strength coefficient B.

Considering the material size-effect caused by the varying IUCT in ball-end milling, a modified Johnson-Cook constitutive law is derived by introducing the strain gradient plasticity based on the Taylor's dislocation principle [33], which can be given as:

$$\tau_s = \tau_{JC}\sqrt{1+\left(\frac{\alpha_c^2 G^2 b_g\sin\varphi_n}{\tau_{JC}^2 t_1}\right)^u} \tag{23}$$

where α_c is a constant, G is the shear modulus, b_g is the magnitude of the Burgers vector, and u is the exponential factor. It is evident from Eq. (23) that the shear stress in the primary shear zone is inversely proportional to the IUCT for a constant shear angle.

Furthermore, the shear force dF_s, which is proportional to the shear stress τ_s in primary shear plane, along with the normal force dN_s can be expressed as:

$$dF_s = \tau_s\frac{dz\cdot t_1}{\cos\lambda_s\sin\varphi_n} \tag{24}$$

$$dN_s = \frac{(tan(\varphi_n-\alpha_n)+\tan\beta_n cos\eta_c)\cos\eta_{sh}}{1-\tan\beta_n\cos\eta_c tan(\varphi_n-\alpha_n)}dF_s \tag{25}$$

In addition, it is well known that there exists an edge radius inevitably on the cutting edge, which can cause an effect of plough forces and contribute to the three differential cutting force components. The plough forces (dP_c, dP_f) can be determined from the slip-line field developed by Waldorf et al. [34]. In this model, the normal rake angle α_n is replaced by effective rake angle α_{ref} depending on the relation between IUCT and edge radius as given below:

$$\alpha_{ref} = \begin{cases} \sin^{-1}(t_1/r_e-1), & t_1 \le t_{lim} \\ \alpha_n, & t_1 > t_{lim} \end{cases} \tag{26}$$

where $t_{lim}=r_e(1+sin\alpha_n)$ is the limiting value of the IUCT and r_e is the edge radius of the cutter.

In short, for the infinitesimal element of the j-th cutting edge, the three differential force components $dF_{t,j}$, $dF_{r,j}$, and $dF_{a,j}$ (tangential, radial, and axial), applied to point P in Fig. 2a, are evaluated from the following matrix form.

$$\begin{Bmatrix} dF_{t,j} \\ dF_{r,j} \\ dF_{a,j} \end{Bmatrix} = \begin{bmatrix} \cos\lambda_s\cos\varphi_n\cos\eta_{sh}+\sin\lambda_s\sin\eta_{sh} & \cos\lambda_s\sin\varphi_n \\ -\sin\varphi_n\cos\eta_{sh} & \cos\varphi_n \\ \sin\lambda_s\cos\varphi_n\cos\eta_{sh}-\cos\lambda_s\sin\eta_{sh} & \sin\lambda_s\sin\varphi_n \end{bmatrix}\begin{Bmatrix} dF_s \\ dN_s \end{Bmatrix} + \begin{bmatrix} \cos\lambda_s & 0 \\ 0 & 1 \\ \sin\lambda_s & 0 \end{bmatrix}\begin{Bmatrix} dP_c \\ dP_f \end{Bmatrix} \tag{27}$$

For the infinitesimal element of the j-th cutting edge, the three differential cutting force components $dF_{t,j}$, $dF_{r,j}$, and $dF_{a,j}$ (tangential, radial, and axial) in LCS, applied to point P

in Fig. 1b, are transformed into TCS using the following matrix relations:

$$\begin{Bmatrix} dF_{x,j} \\ dF_{y,j} \\ dF_{z,j} \end{Bmatrix} = \begin{bmatrix} -\cos\varphi_j & -\sin\varphi_j\sin\kappa & -\sin\varphi_j\cos\kappa \\ \sin\varphi_j & -\cos\varphi_j\sin\kappa & -\cos\varphi_j\cos\kappa \\ 0 & \cos\kappa & -\sin\kappa \end{bmatrix} \begin{Bmatrix} dF_{t,j} \\ dF_{r,j} \\ dF_{a,j} \end{Bmatrix} \tag{28}$$

The differential cutting forces are integrated along the in-cut portion of the j-th cutting edge, and the total cutting forces produced by this cutting edge can be obtained as:

$$F_q[\varphi_j(z)] = \int_{z_1(\varphi_j)}^{z_2(\varphi_j)} dF_q[\varphi_j(z)]dz, \quad q = x,y,z \tag{29}$$

where $z_1(\varphi_j)$ and $z_2(\varphi_j)$ are the lower and upper axial engagement limits of the in-cut portion.

Finally, the cutting forces contributed by all cutting edges are summed to obtain the total instantaneous forces on the cutter as:

$$\begin{aligned} F_x(\varphi) &= \sum_{j=1}^{N_t} F_{x,j}[\varphi(z)], \quad F_y(\varphi) \\ &= \sum_{j=1}^{N_t} F_{y,j}[\varphi(z)], \quad F_z(\varphi) = \sum_{j=1}^{N_t} F_{z,j}[\varphi(z)] \end{aligned} \tag{30}$$

3.2 IUCT with cutter runout

The cutter runout is a common phenomenon in multi-fluted milling operations [35]; the detailed procedure to calculate the IUCT is illustrated in Fig. 3. O_k and O'_k are the ideal cutter axis center and the spindle rotational center of the element k, and their distance $\|O_kO'_k\|$ is the runout amplitude ρ. The runout angle λ is defined to be the angle between the direction $\overrightarrow{O_kO'_k}$ and the negative Y-axis direction. When the cutter runout exists, each point of the cutting edge experiences a different IUCT as predicted in Eq. (6). The IUCT generated by a cutting point depends on the effective radius of the cutting edge and the effective radius of the other cutting edges as well.

From the geometrical relation in Fig. 3, the effective radius of the infinitesimal element k of the i-th cutting edge at elevation z can be given as:

$$R_{i,k}(z) = R(z) + \rho cos\left[\lambda - \psi(z) - (i-1)\varphi_p\right] \tag{31}$$

where $R_{i,k}(z)$ and $R(z)$ are the actual and ideal cutting radius of the element k, respectively.

The actual cutting radius changes in Eq. (31) due to the cutter runout, and redistributes the IUCT. Therefore, from the right picture of Fig. 3, the IUCT of the infinitesimal element k on the i-th cutting edge at elevation z can be calculated as [35]:

$$h^c_{i,k}(\varphi) = m_i f_t \sin\theta_{i,k}(\varphi) + R_{i,k}(z) - R_{i-m_i,k}(z) \tag{32}$$

where m_i is the i-th cutting edge is removing the material left by the m_i -th cutting edge.

For a N_t -flute ball-end cutter, N_t candidates of the IUCT can be calculated using Eq. (32). The correct IUCT is the small positive one of the N_t candidates, i.e.,

$$h^0_{i,k}(\varphi) = \min\left(h^c_{1,k}(\varphi), h^c_{2,k}(\varphi), ..., h^c_{N_t,k}(\varphi)\right) \tag{33}$$

However, all the candidates are negative due to the cutter runout and the correct IUCT can be considered as zero.

In addition, the local cutting velocity is then calculated as:

$$V = 2\pi n_r \cdot R_{i,k}(z) \tag{34}$$

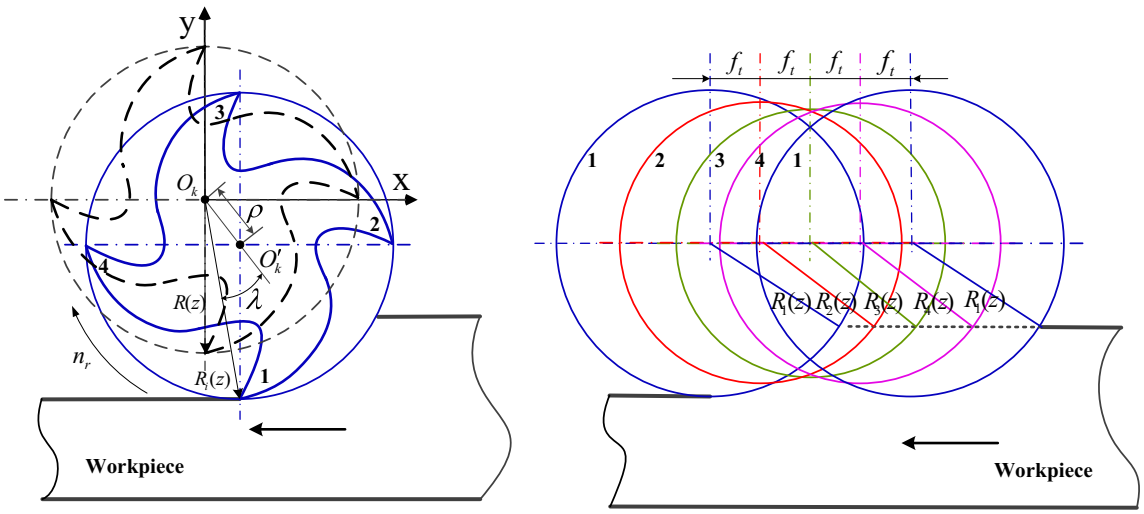

Fig. 3 Cutter runout and tooth path trajectories

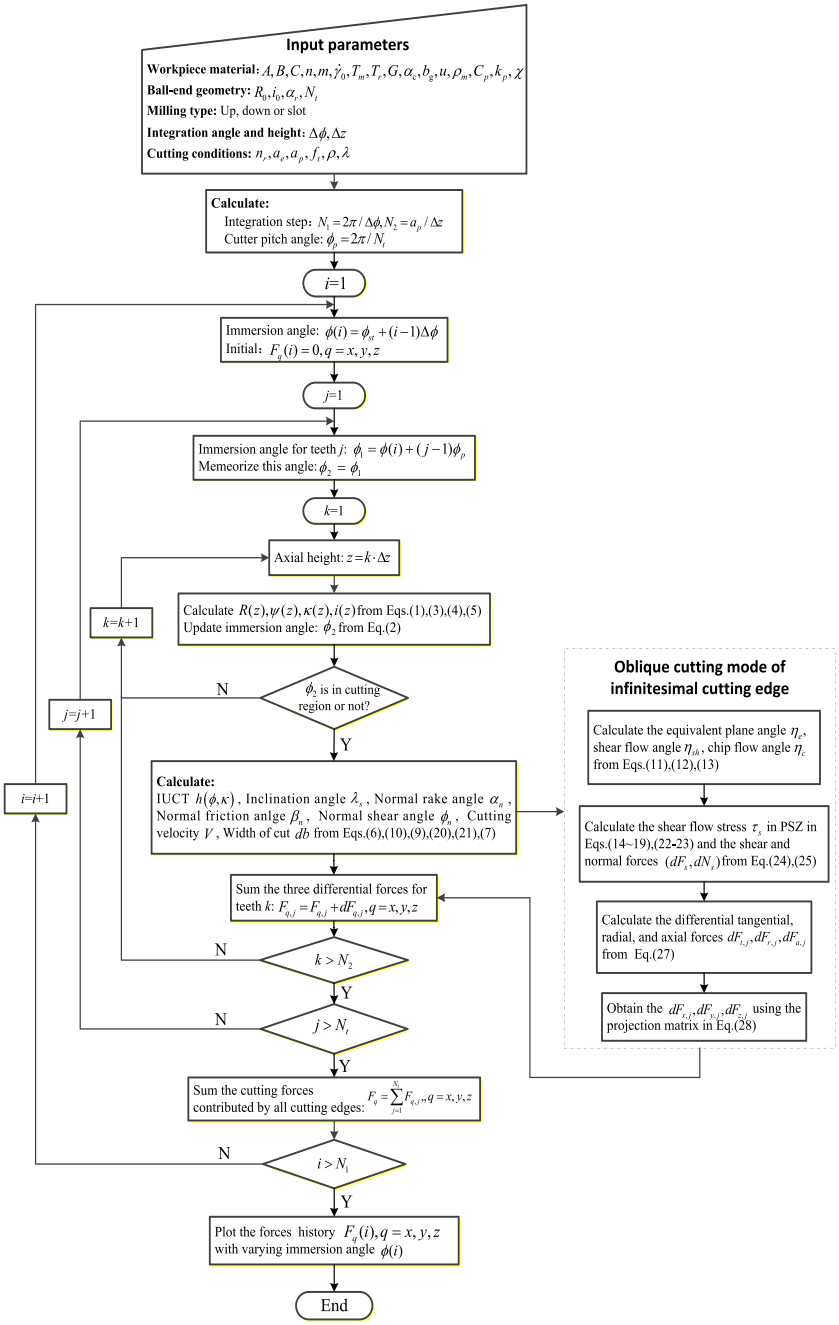

Fig. 4 The flow chart of cutting forces calculation

Table 1 Properties of workpiece material Ti6Al4V [37]

(1) Johnson-Cook parameters

A	B	C	n	m	γ_0	T_m	T_r
862.5 MPa	331.2 MPa	0.0120	0.34	0.8	1 s^{-1}	1933 K	293 K

(2) Thermo-physical properties

Density ρ_m	Heat capacity C_p	Thermal conductivity k_p	Taylor-Quinney coefficient χ
4430 kg/m^3	526 J/(kgK)	7 W/(mK)	0.85

(3) Mechanical properties

Shear modulus G	α_c	b_g	u
44 GPa	0.5	0.304	1

Table 2 Cutting conditions and tool geometry used in [11]

Case	Spindle speed n_r (rpm)	Feed per teeth f_t (mm/z)	Depth of cut a_p (mm)	Tool diameter D (mm)	Rake angle α_r (deg)	Type
1	269	0.0508	1.27	19.05	0	Slot
2	269	0.0508	6.35	19.05	0	Slot
3	269	0.1016	3.81	19.05	5	Slot
4	269	0.0762	3.048	12.7	10	Slot
5	269	0.0508	6.35	19.05	0	Half-immersion
6	269	0.102	6.35	19.05	0	Half-immersion

From Eqs. (31) and (32), the variation of the cutting radius causes the cutting velocity to change, and the normal rake angle α_n and the edge inclination angle λ_s slightly change. All these angle variations have no significant effect on the cutting forces and then are neglected in this proposed model.

Finally, due to the relatively large number of equations associated with the proposed analytical force model of ball-end milling, a solving procedure is given as shown in Fig. 4. In addition, when the cutter runout is considered, the IUCT and cutting velocity are modified according to Eqs. (32) and (34).

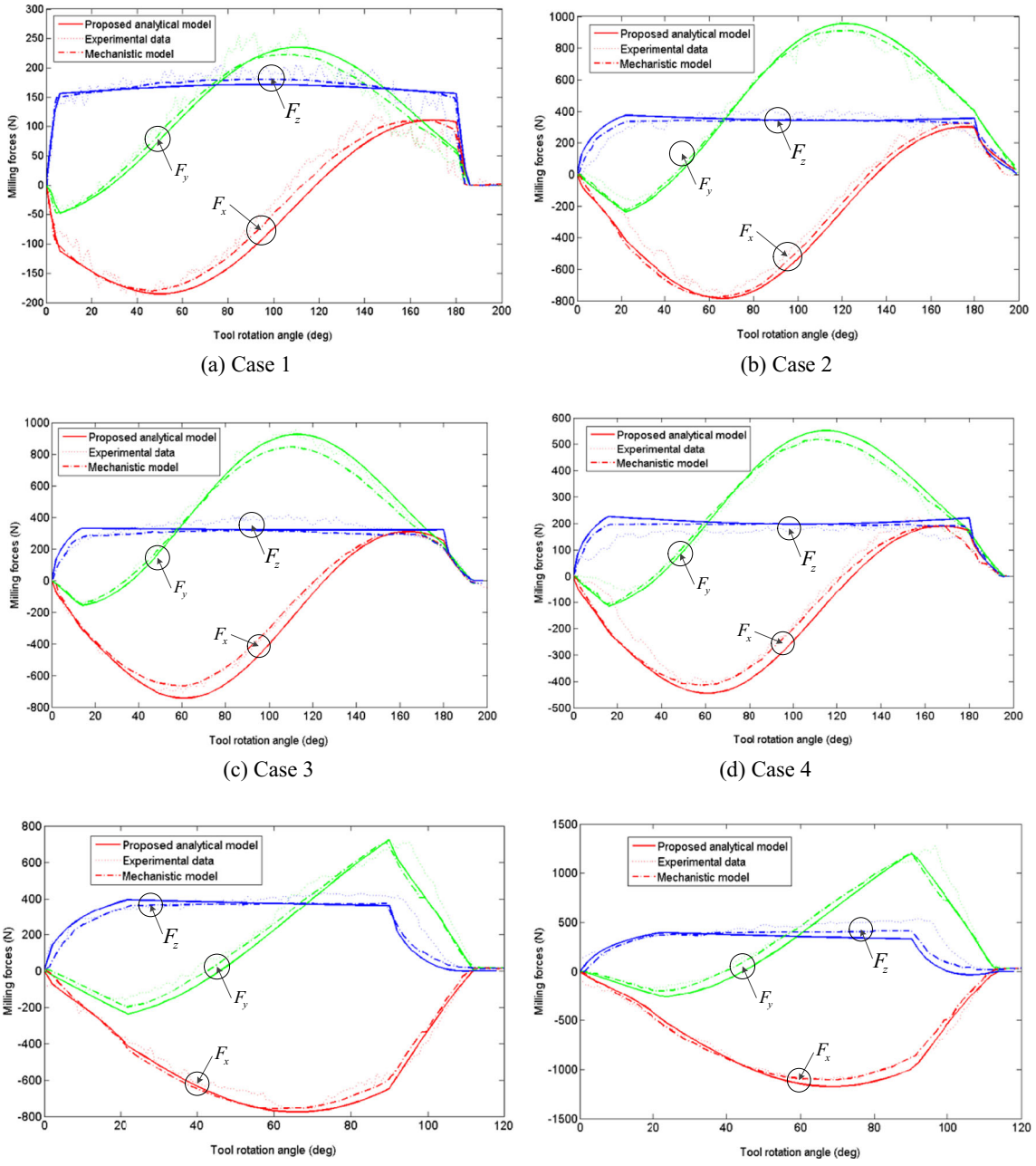

(a) Case 1 (b) Case 2

(c) Case 3 (d) Case 4

(e) Case 5 (f) Case 6

Fig. 5 Comparison of cutting forces between the analytical model and the published results

4 Model validation

In order to validate the effectiveness of the proposed analytical model of cutting forces for ball-end milling, we firstly compare with the published results obtained by Lee et al. [11] and then demonstrate that the model is suitable for various cutting conditions. Furthermore, a series of the ball-end milling experiments are carried out with the aim to verify the proposed model. And the corresponding computer programs in MATALAB 7.9 are developed to implement on the analysis of cutting force model.

4.1 Comparison with the published results

In this section, the published results obtained from the mechanistic model and experimental data [11] are selected for comparison, in which two types of milling tests, i.e., slot milling and half radial immersion milling, are carried out. The behavior of the used workpiece material Ti6Al4V is described by the modified Johnson-Cook constitutive law in Eqs. (22) and (23). Table 1 gives the properties of workpiece material.

The carbide ball-end cutters used have single-flute cutting edge, 30^0 nominal helix angle, and two different diameters (12.7 and 19.05 mm), in which the rake angles range from 0^0 to 15^0. The other tool geometry and cutting conditions are listed in Table 2.

The proposed analytical model utilizes the same constants of the workpiece material, cutting conditions, and tool geometry. The involved mean friction angle β_n can be obtained from Eq. (20), where the sliding friction coefficient $\mu_s=0.326+1.1\times10^{-3}V_c(m/min)$ for this tool-workpiece pair [31]. The material constant in Eq. (21) is $C_1=0.785$ rad, $C_2=0.5$ [26]. The edge force coefficients are determined from the orthogonal experiments and their values are $K_{te}=24$ N/mm, $K_{re}=43$ N/mm. In addition, the cutter runout is not considered in this comparison for the single-flute milling.

Figure 5a–f show the comparison of cutting forces obtained by the proposed analytical model and the published results. It

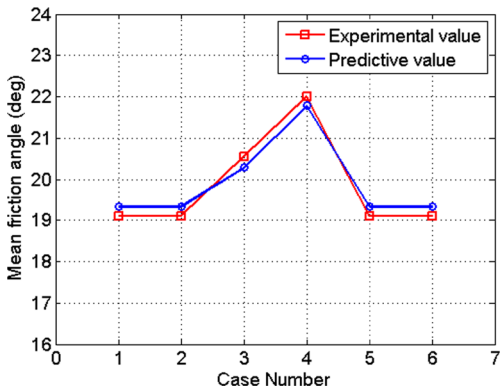

Fig. 6 Comparison of mean friction angles between predicted and experimental values

Fig. 7 Experimental setup

can be observed that the cutting forces calculated in this work are in good agreement with the published results obtained by the mechanistic model and experimental data [11]. However, there exists a small deviation on the amplitude of the maximum cutting forces between the proposed analytical model and the published results. This deviation might be attributed to the cutter deflection which is not considered in the proposed model.

Furthermore, the mean shear flow stress τ_{JC} predicted with the proposed model in the primary shear zone is about 592 MPa and very close to the value 613 MPa of the orthogonal cutting database in [11]. Due to this low spindle speed, the sliding friction coefficient can be taken as 0.33 here. The mean friction is also in agreement with the experimental values [11], $\beta_n=19.1+0.29\alpha_n(\text{deg})$, as shown in Fig. 6.

4.2 Experimental validation

In order to further verify the proposed force model, a series of ball-end milling tests have been performed on a vertical 5-axis machining center without cutting fluid and the experimental setup is shown as in Fig. 7. The workpiece is mounted on a three-component Kistler table dynamometer (model 9523B) which is used to measure cutting forces. A carbide ball-end mill (reference 1B230-1200-XA 1630) with two flutes, 12-mm diameter, 30^0 helix angle, 5^0 normal rake angle, and 0.02-mm edge radius is used in these tests. The pre-finished workpiece is NAB (nickel aluminum bronze) material and its chemical composition is listed in Table 3.

Table 3 The chemical composition of NAB

Element	Cu	Al	Fe	Ni	Mn	Others
wt%	80.3	9.28	4.45	4.24	1.42	≤0.03

Table 4 Cutting conditions used for ball-end milling tests

Case	Spindle speed n_r (rpm)	Feed per teeth f_t (mm/z)	Radial width of cut a_e (mm)	Axial depth of cut a_p (mm)	Type
1	800	0.12	4	2	Down
2	800	0.16	–	1.2	Slot
3	1500	0.04	6	1.2	Up
4	1500	0.08	–	1	Slot

In addition, the flow behavior of the material NAB is described by the modified Johnson-Cook constitutive law and its involved parameters are given as:

A=295 MPa, B=759.5 MPa, C=0.011, n =0.405, m=1.09, γ_0=0.001, T_m=1311 K, T_r=298 K
G=117 GPa; αc=0.5; bg=0.414; u=1.2;

And the material density ρ is 7530 kg/m^3, the heat capacity C_p is 419 J/(kgK), and Taylor-Quinney coefficient χ=0.85.

More than 40 milling tests are conducted, and three types of milling, i.e., up, down, and slot, are selected at different feed rates and axial depths of cut. Four types of cutting conditions for the tests and simulations are summarized in Table 4.

Table 5 The runout parameters in proposed analytical model

Case	Runout amplitude ρ (mm)	Runout angle λ (deg)
1	0.0013	1.5
2	0.0025	30
3	0.0034	60
4	0.0032	30

The mean friction angle β_n is obtained from Eq. (20), where the sliding friction coefficient μ_s=0.654$V_c^{-0.208}$ for this calculation. The material constant in Eq. (18) is C_1=0.698 rad, C_2=0.5.

The instantaneous milling forces for one revolution of the cutter can be obtained by taking the average values of cutting forces measured in the neighboring 10 periods, and then compare with the ones predicted from the proposed analytical force model. The results of comparison are shown in Fig. 8a–d.

It can be seen from Fig. 8 that the cutter runout phenomenon exists in the multi-fluted milling process. The unknown runout parameters can be calculated by the one-dimensional search method, in which then the minimum variance is obtained from comparing the corresponding instantaneous cutting forces by changing the runout amplitude and angle with the experimental values. The detailed method can be referred to

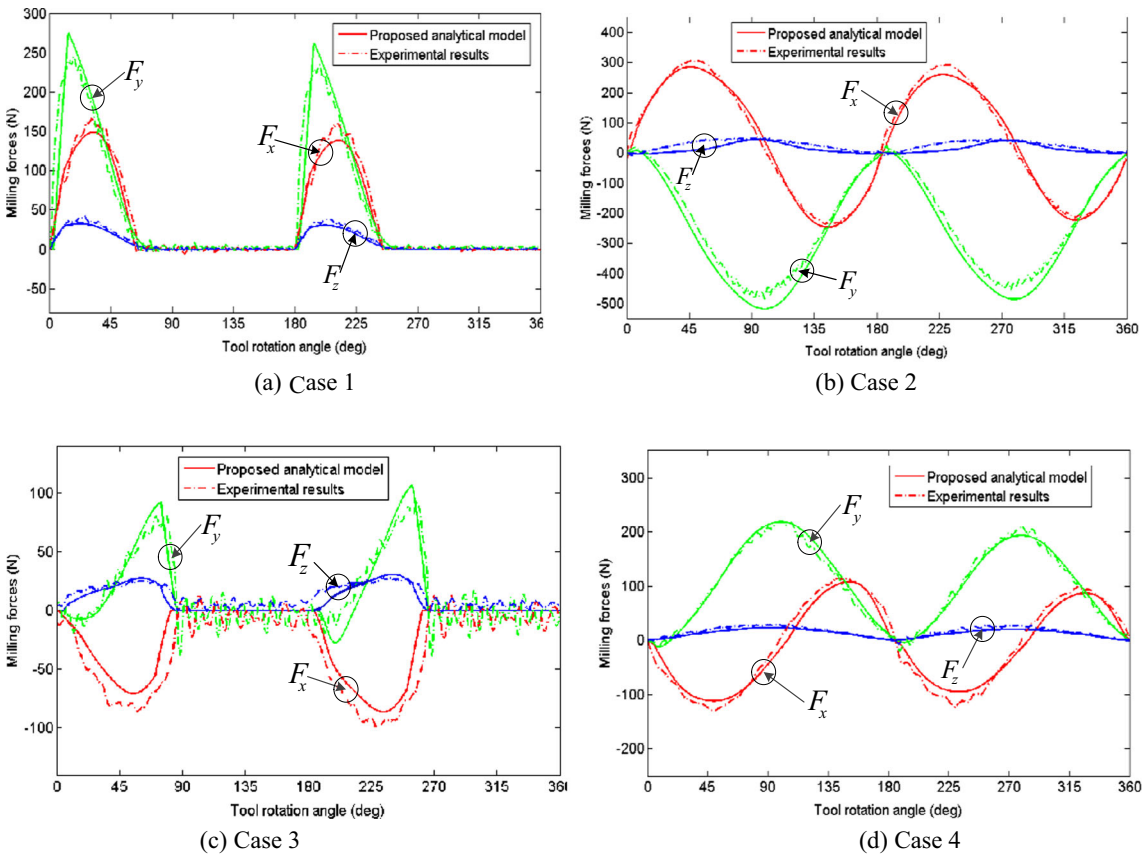

(a) Case 1 (b) Case 2

(c) Case 3 (d) Case 4

Fig. 8 Comparison of proposed analytical model and experimental results

the literature [36]. Table 5 gives the identified runout parameters.

What is more, Fig. 8 also shows that under these cutting conditions, the experimental values of milling forces have a good agreement with the proposed analytical model on the waveform, amplitude, and phase. And the average and peak errors are less than 16 and 22 %, respectively. The main reasons for this deviation may be attributed to: (1) although the cutter runout is considered in the proposed analytical model, the cutter deflection is caused by the peak forces due to the stiffness in actual ball-end milling process. In addition, the plough forces are introduced at the tool-workpiece interface zone due to the little flank wear of the cutter. (2) In the proposed model, the predicted results are influenced due to the errors caused by the some measured or identified parameters.

5 Conclusions

In this paper, an analytical force model considering cutter runout for ball-end milling has been developed and discussed based on a predictive machining theory, which is verified the effectiveness by the published results and experimental data. The contributions of the proposed analytical model are drawn as follows:

(1) The analytical model puts the workpiece material properties, tool geometry, cutting conditions, and the type of milling as the input data and regards the cutting action of each infinitesimal element on the cutting edge as the classical oblique cutting process in which the cutting force components are calculated using the predictive oblique cutting model.
(2) A modified Johnson-Cook constitutive law is introduced to calculate the shear flow stress, which considers not only the strain hardening and thermal softening but also the material size-effect, i.e., strain gradient effect.
(3) The chip geometry of ball-end cutter is analyzed, and the account has been taken into the effect of the edge radius, varying sliding friction coefficient, and cutter runout on the cutting forces in the proposed analytical model.
(4) The predicted results for cutting forces are in good agreement with the published results and experimental data, which shows that the proposed analytical model is efficient and suitable. In addition, the proposed model is easy to implement, as a priority to the mechanistic model, and can easily be extended to other workpiece materials and machining operations such as turning and drilling.

However, the effect of deflection and plough forces are caused by the stiffness and flank wear of the cutter, respectively, in actual ball-end milling process need to be studied in future work for more accurate prediction of cutting forces.

Acknowledgments This work was partially supported by the National Basic Research Program of China (2014CB046704) and the National Natural Science Foundation of China (51375182), the National Science & Technology Pillar Program of China(2014BAB13B01).

References

1. Altintas Y (2012) Manufacturing automation: metal cutting mechanics, machine tool vibrations, and CNC design. Cambridge university press
2. Cheng K (2012) Machining Dynamics: fundamentals, application and practices. Springer
3. Kline WA, Devor R (1983) The effect of runout on cutting geometry and forces in end milling. Int J Mach Tool Des Res 23(2):123–140
4. Fu H, Devor RE, Kapoor SG (1984) A mechanistic model for the prediction of the force system in face milling operations. ASME J Manuf Sci Eng 106(1):81–88
5. Endres WJ, Devor RE, Kapoor SG (1995) A dual-mechanism approach to the prediction of machining forces, part 1: model development. ASME J Manuf Sci Eng 117(4):526–533
6. Engin S, Altintas Y (2001) Mechanics and dynamics of general milling cutters. Part I: helical end mills. Int J Mach Tools Manuf 41(15):2195–2212
7. Gradišek J, Kalveram M, Weinert K (2004) Mechanistic identification of specific force coefficients for a general end mill. Int J Mach Tools Manuf 44(4):401–414
8. Lim EM, Feng HY, Menq CH, Lin ZH (1995) The prediction of dimensional error for sculptured surface productions using the ball-end milling process. Part 1: chip geometry analysis and cutting force prediction. Int J Mach Tools Manuf 35(8):1149–1169
9. Yang M, Park H (1991) The prediction of cutting force in ball-end milling. Int J Mach Tools Manuf 31(1):45–54
10. Budak E, Altintaş Y, Armarego EJA (1996) Prediction of milling force coefficients from orthogonal cutting data. ASME J Manuf Sci Eng 118(2):216–224
11. Lee P, Altintas Y (1996) Prediction of ball-end milling forces from orthogonal cutting data. Int J Mach Tools Manuf 36(9):1059–1072
12. Armarego EJA (1994) Force prediction models and CAD/CAM software for helical tooth milling processes. III. End-milling and slotting operations. Int J Prod Res 32(7):1715–1738
13. Li Z, Niu J, Wang X, Zhu L (2015) Mechanistic modeling of five-axis machining with a general end mill considering cutter runout. Int J Mach Tools Manuf 96:67–79
14. Habibi M, Arezoo B, Nojedeh MV (2011) Tool deflection and geometrical error compensation by tool path modification. Int J Mach Tools Manuf 51(6):439–449
15. Tyler CT, Schmitz TL (2013) Analytical process damping stability prediction. J Manuf Process 15(1):69–76
16. Zhang L, Feng J, Wang Y, Chen M (2009) Feedrate scheduling strategy for free-form surface machining through an integrated geometric and mechanistic model. Int J Adv Manuf Technol 40(11–12):1191–1201
17. Merchant ME (1945) Mechanics of the metal cutting process. I. Orthogonal cutting and a type 2 chip. J Appl Physiol 11:168–175
18. Armarego EJA (1993) Force prediction models and CAD/CAM software for helical tooth milling processes. II. Peripheral milling operations. Int J Prod Res 31(10):2319–2336

19. Oxley PLB (1989) The mechanics of machining: an analytical approach to assessing machinability. Ellis Horwood Publisher, New York
20. Lalwani D, Mehta N, Jain P (2009) Extension of Oxley's predictive machining theory for Johnson and Cook flow stress model. J Mater Process Technol 209(12):5305–5312
21. Young H, Mathew P, Oxley PLB (1994) Predicting cutting forces in face milling. Int J Mach Tools Manuf 34(6):771–783
22. Li HZ, Zhang WB, Li XP (2001) Modelling of cutting forces in helical end milling using a predictive machining theory. Int J Mech Sci 43:1711–1730
23. Li XP, Nee AYC, Wong YS, Zheng HQ (1999) Theoretical modelling and simulation of milling forces. J Mater Process Technol 89: 266–272
24. Zheng HQ, Li XP, Wong YS, Nee AYC (1999) Theoretical modelling and simulation of cutting forces in face milling with cutter runout. Int J Mach Tools Manuf 39(12):2003–2018
25. Pang L (2012) Analytical modelling and simulation of metal cutting forces for engineering alloys: UMI Dissertations Publishing
26. Moufki A, Dudzinski D, Le Coz G (2015) Prediction of cutting forces from an analytical model of oblique cutting, application to peripheral milling of Ti-6Al-4V alloy. Int J Adv Manuf Technol 1–12
27. Li B, Hu Y, Wang X, Li C, Li X (2011) An analytical model of oblique cutting with application to end milling. Mach Sci Technol 15(4):453–484
28. Fu Z, Yang W, Wang X, Juergen L (2015) Analytical modelling of milling forces for helical end milling based on a predictive machining theory. Proc CIRP 31:258–263
29. Arrazola PJ, Ozel T, Umbrello D, Davies MJ (2013) Recent advances in modelling of metal machining processes. CIRP Ann 62(2):695–718
30. Li B, Wang X, Hu Y, Li C (2011) Analytical prediction of cutting forces in orthogonal cutting using unequal division shear-zone model. Int J Adv Manuf Technol 54(5–8):431–443
31. Budak E, Ozlu E (2008) Development of a thermomechanical cutting process model for machining process simulations. CIRP Ann 57(1):97–100
32. Ozlu E, Budak E, Molinari A (2009) Analytical and experimental investigation of rake contact and friction behavior in metal cutting. Int J Mach Tools Manuf 49(11):865–875
33. Joshi SS, Melkote SN (2004) An explanation for the size-effect in machining based on strain gradient plasticity. Trans ASME J Manuf Sci Eng 126(4):679–684
34. Waldorf DJ, Devor RE, Kapoor SG (1998) A slip-line field for ploughing during orthogonal cutting. Trans ASME J Manuf Sci Eng 120(4):693–699
35. Wang JJ, Liang SY (1996) Chip load kinematics in milling with radial cutter runout. Trans ASME J Manuf Sci Eng 118(1):111–116
36. Ko JH, Cho DW (2005) 3D ball-end milling force model using instantaneous cutting force coefficients. Trans ASME J Manuf Sci Eng 127(1):1–12
37. Meyer HW, Kleponis DS (2001) Modeling the high strain rate behavior of titanium undergoing ballistic impact and penetration. Int J Impact Eng 26(1):509–521